LowContent Ru Catalysts for Efficient CO2 Methanation

ChemCatChem

Research Article
doi.org/10.1002/cctc.202501275

Chemistry Europe
European Chemical Societies Publishing

www.chemcatchem.org

Low-Content Ru Catalysts for Efficient CO_2 Methanation

Andrea Rizzetto[†],[a] Marco Pietro Mezzapesa[†],[a] Fabrizio Celoria[†],[a] Fabio Salomone,*[a] Enrico Sartoretti,*[a] Marco Piumetti,[a] Raffaele Pirone,[a] and Samir Bensaid*[a]

A series of low-content Ru-based catalysts supported on Al_2O_3, TiO_2, CeO_2, MgO, and ZrO_2 were synthesized via incipient wetness impregnation and evaluated for CO_2 methanation. Among them, Ru/TiO_2 exhibited the highest activity in terms of turnover frequency (TOF = 3.35 s^{-1}) and selectivity toward CH_4 (> 95%). To elucidate the underlying reaction mechanism, *operando* Diffuse Reflectance Infrared Fourier Transform Spectroscopy (DRIFTS) analyses were performed, revealing the presence of key surface intermediates. Based on these observations, several power-law and Langmuir–Hinshelwood–Hougen–Watson (LHHW) kinetic models were formulated and fitted to experimental data. A detailed comparison of different mechanistic hypotheses was conducted, highlighting the role of CO_2 dissociation and stepwise hydrogenation pathways. A two active site model that considers CO_2 adsorption on the basic sites of the support and the continuation of the reaction by hydrogen spillover from Ru nanoparticles provided the best agreement with experimental results. Overall, the combination of catalytic testing, operando spectroscopy, and kinetic modeling offers a comprehensive understanding of the CO_2 methanation pathway over Ru/TiO_2 and provides a reliable basis for catalyst comparison and reactor design to effectively manage thermal issues.

1. Introduction

The Sabatier reaction has gathered growing attention as a promising route to valorize CO_2 and renewable H_2 to produce synthetic natural gas as sustainable energy carrier to reduce society's dependency on fossil fuels. The three main reactions involved in the process are the hydrogenation of CO_2 and CO to CH_4 (Equations 1 and 2) and the RWGS reaction (Equation 3).

$$CO_{2(g)} + 4\,H_{2(g)} \leftrightarrows CH_{4(g)} + 2\,H_2O_{(g)} \qquad \Delta_r\tilde{H}^0_{298K} = -165\ \text{kJ/mol}\ \Delta_r\tilde{G}^0_{298K} = -114\ \text{kJ/mol} \tag{1}$$

[a] Dr. A. Rizzetto[†], M. P. Mezzapesa[†], F. Celoria[†], Dr. F. Salomone, Dr. E. Sartoretti, Prof. M. Piumetti, Prof. R. Pirone, Prof. S. Bensaid
Department of Applied Science and Technology (DISAT), Politecnico di Torino, Corso Duca degli Abruzzi 24, Torino 10129, Italy
E-mail: fabio.salomone@polito.it
enrico.sartoretti@polito.it
samir.bensaid@polito.it

Abbreviations: BET, Brunauer-Emmett-Teller; BJH, Barrett–Joyner–Halenda; DFT, Density Functional Theory; DRIFTS, Diffuse Reflectance Infrared Fourier Transform Spectroscopy; EDS, Energy-Dispersive X-ray Spectroscopy; FESEM, Field-Emission Scanning Electron Microscope; FTIR, Fourier-Transform Infrared; GHSV, Gas Hourly Space Velocity (h^{-1}); HAADF, High-Angle Annular Dark-Field; HR, High Resolution; LHHW, Langmuir–Hinshelwood–Hougen–Watson; LK-WI, Lunde-Kester Water Inhibition kinetic model; MCT, Mercury Cadmium Telluride; NDIR, Non-Dispersive Infrared; OF, Objective Function; PDF, Powder Diffraction File; PL, Power-Law kinetic model; RWGS, Reverse Water Gas Shift; STEM, Scanning Transmission Electron Microscopy; TCD, Thermal Conductivity Detector; TEM, Transmission Electron Microscopy; TOF, Turnover frequency (s^{-1}); TPD, Temperature-Programmed Desorption; TPR, Temperature-Programmed Reduction; XRD, X-Ray Diffraction; YSZ, Yttria-Stabilized Zirconia; $\bar{c}_{p,g}$, Molar specific heat capacity of the gas mixture (J mol^{-1} K^{-1}); D_{Ru}, Ruthenium dispersion (dimensionless); $d_{t,i}$, Internal tube diameter (0.0525 m); $d_{t,o}$, External tube diameter (0.0603 m); E_A, Activation energy (J mol^{-1}); k, Arrhenius' kinetic constant; K_{eq}, Equilibrium constant of the CO_2 methanation (bar^{-2}); K_i, Van't Hoff adsorption term; K_{i,T_0}, Pre-exponential factor of the i-th van't Hoff term at T_0; k_{T_0}, Pre-exponential factor of the Arrhenius' kinetic term at T_0; L_t, Total length of the catalytic bed (m); L_{Ru/TiO_2}, Length of the Ru/TiO_2 catalytic bed (m); m, Coefficient of the water inhibition term in the LK-WI model (bar^{-1}); M_i, Molecular weight of the i-th species (kg mol^{-1}); m_{Ru}, Ru mass loading (nominal value = 0.0025 kg Ru kg^{-1}); n, Exponent in the LK-WI model (dimensionless); N_c, Total number of components; n_{CO_2}, Exponent of the partial pressure for the CO_2 in the PL model (dimensionless); N_e, Total number of experiments; n_{H_2}, Exponent of the partial pressure for the H_2 in the PL model (dimensionless); $\dot{n}_{i,in}$, Inlet molar flowrate of the i-th species (mol s^{-1}); $\dot{n}_{i,out}$, Outlet molar flowrate of the i-th species (mol s^{-1}); N_r, Total number of reactions (= 1, only CO_2 methanation); $n_{Ru/CO}$, Ru-CO stoichiometric coefficient during CO chemisorption (= 1); p_i, Partial pressure of the i-th component (bar); Q, Reaction quotient of the CO_2 methanation (bar^{-2}); R, Ideal gas constant (8.314 J mol^{-1} K^{-1}); r_i, Molar reaction rate of the i-th component (mol kg^{-1} s^{-1}); T, Temperature (K); T_c, Temperature of the coolant medium (K); T_0, Reference temperature (598.15 K); U, Overall heat transfer coefficient (W m^{-2} K^{-1}); $\tilde{v}$, Standard molar volume of the gas (0.022414 m^3 mol^{-1}); V_{ads}, Adsorbed volume of gas (m^3 kg^{-1}); v_z, Superficial gas velocity along the axial coordinate z (m s^{-1}); w_{Ru}, Mass fraction of Ru in the catalyst (g Ru g_{cat}^{-1}); $y^{exp}_{i,j}$, Experimental molar fraction of the i-th species for the j-th experiment (dimensionless); $y^{mod}_{i,j}$, Modeled molar fraction of the i-th species for the j-th experiment (dimensionless); z, Axial coordinate (m); $\Delta_r\tilde{G}^0_{298K}$, Molar Gibbs' free energy variation of the reaction at 25 °C and 1 bar (kJ mol^{-1}); ΔH_i, Adsorption enthalpy of the i-th component (J mol^{-1}); $\Delta_r\tilde{H}_\alpha$, Molar enthalpy of reaction of the key component of the α-th reaction (J mol^{-1}); $\Delta_r\tilde{H}^0_{298K}$, Molar enthalpy variation of the reaction at 25 °C and 1 bar (kJ mol^{-1}); ε_b, Bed void fraction of the catalytic bed (dimensionless); ε_t, Total void fraction of the reactor (dimensionless); ζ_{CO_2}, CO_2 conversion (dimensionless); η_{CH_4}, CH_4 yield (dimensionless); $\nu_{i,\alpha}$, Stoichiometric coefficient of the i-th component for the α-th reaction (dimensionless); ρ_g, Density of the gas mixture (kg m^{-3}); ρ_i, Density of the i-th chemical species (kg m^{-3}); ρ_s, Apparent skeletal density of the catalyst in the diluted catalytic bed (kg m^{-3}); σ_i, Selectivity of the i-th species.

[†] *These authors contributed equally to this work.*

Supporting information for this article is available on the WWW under https://doi.org/10.1002/cctc.202501275

$$CO_{(g)} + 3\,H_{2(g)} \leftrightarrows CH_{4(g)} + H_2O_{(g)}$$
$$\Delta_r\tilde{H}^0_{298K} = -206\ \text{kJ/mol}\,\Delta_r\tilde{G}^0_{298K} = -142\ \text{kJ/mol} \quad (2)$$

$$CO_{2(g)} + H_{2(g)} \leftrightarrows CO_{(g)} + H_2O_{(g)}$$
$$\Delta_r\tilde{H}^0_{298K} = 41\ \text{kJ/mol}\,\Delta_r\tilde{G}^0_{298K} = 29\ \text{kJ/mol} \quad (3)$$

The overall process is strongly exothermic due to the high enthalpy of reaction and equilibrium conversion, and its thermal management is critical due to the fast reaction rates. Transitional metals of groups VIII-X are commonly employed for CO_2 hydrogenation and, more specifically, Ru-based and Ni-based catalysts are the most studied systems. Although Ni-based catalysts exhibit good activity and are cheaper than Ru-based catalysts, the latter demonstrate extremely high activity at low temperatures and lower energies of activation, that could be exploited to thermally manage the methanation reaction.

The performance of supported Ru catalysts strictly depends on the physicochemical properties of the support, that modulates metal dispersion, particle morphology, electronic and acid-base properties, reducibility, and metal-support interactions. In 1981, Solymosi et al.[1] were among the first to investigate the effects of different supports during CO_2 methanation, revealing that Ru/TiO_2 showed the highest CO_2 uptake, followed by Ru/MgO and Ru/Al_2O_3, while Ru/SiO_2 exhibited negligible uptake, suggesting weak metal-support interactions and low activity. Its limited activity has been later confirmed by Panagiotopoulou et al.,[2] while other systems (i.e., Ru/TiO_2, $Ru/CeO_2/Al_2O_3$ and Ru/YSZ) have outperformed the SiO_2-supported Ru catalyst.[2] Supports like CeO_2 and MnO_x, studied by Dreyer et al.,[3] displayed amphoteric properties and high reducibility, enhancing H_2 activation via spillover.[3] An excessive reducibility could however weaken the CO interactions, as observed for ZnO and CeO_2 supports, shifting the product yield from CH_4 to CO via RWGS reaction.[3] Other authors have pointed out that Ru loading should be optimized because too little Ru limits CO_2 adsorption, while excess loading worsens the hydrogenation process.[4]

A recurring theme across literature is the role of TiO_2 as support for Ru-based catalysts. It was first identified as the most active and selective toward CH_4 in mild conditions (200–250 °C).[1,2] Then, more recent studies showed the effect of different TiO_2 crystal phases and metal dispersion. Li et al.[5] have revealed that shifting from rutile-TiO_2 to anatase-TiO_2 could invert the selectivity from CH_4 to CO. This phenomenon was ascribed to a phase-dependent hydrogen spillover that most likely changes the adsorption and activation of the CO intermediate.[5] Subsequently, Zhao et al.[6] and Zhou et al.[7] further revealed that Ru preferentially grows on rutile-TiO_2 crystal domains forming flat anchored Ru particles showing enhanced CH_4 yield, while Ru forms more spherical clusters on anatase-TiO_2 interface resulting in poor activity. More recently, Yang et al.[8] have confirmed the structural shape-selective activity of Ru facets: planar (0001) surfaces exhibit higher activity than corrugated $(10\bar{1}1)$ facets. Lastly, Cimino et al.[9] have shown that mixed TiO_2 phases (i.e., anatase and brookite) boosted the reaction rates improving Ru dispersion.[9]

All those insights into support effects should ultimately converge into a coherent reaction mechanism able to rationalize how structural and electronic properties at the metal-support interface govern the performance and the kinetic behavior of the catalysts. In 1973, Lunde and Kester[10] developed a pioneering power-law kinetic model to describe CO_2 methanation under a wide range of operative conditions on 0.5 wt.% Ru/Al_2O_3. The role of surface intermediates remained unclear without mechanistic study, and over the decades, several authors would opt for a simplified power-law kinetic model.[11] However, eight years later, Solymosi et al.[1] carried out a groundbreaking IR spectroscopic study on four supported Ru-based catalysts (i.e., Ru/Al_2O_3, Ru/MgO, Ru/SiO_2 and Ru/TiO_2) paving the way for further advancements. They have identified the formation of formate (HCOO*) species during H-assisted CO_2 adsorption and have proposed its further hydrogenation into carbonyl (CO*) species. As the metal-carbon bond is stronger than the carbon-oxygen bond they have proposed a dissociative carbon mechanism, that was supported by the works of Weatherbee and Bartholomew in the next three years.[12,13] In 1994, Marwood et al.[14] employed transient DRIFTS measurements to build a microkinetic CO_2 methanation model and identify the reaction pathway on 2 wt.% Ru/TiO_2. They demonstrated the formation of bicarbonate ($HOCO_2$*) species, that are further converted into formates (HCOO*) only in the presence of both H_2 and Ru.[14] This finding implied that H_2 is necessary for activating key intermediates, with CO* formation emerging as rate-determining step (RDS).[14] Later, in 2018, Falbo et al.[11] have confirmed that water inhibits the overall CO_2 methanation, while H_2 favors the formation of CO* species on a 0.5 wt.% Ru/Al_2O_3 catalyst, reinforcing the competitive adsorption phenomena suggested by Marwood et al.[14] Those observations have laid the conceptual foundation to discriminate between reactive intermediate and spectator species. Two years earlier, Wang et al.[15] have indeed thoroughly investigated the CO_2 methanation on 0.5 wt.% and 5 wt.% Ru/Al_2O_3, proposing an associative CO_2 adsorption mechanism followed by two possible reaction pathways: a dissociative carbon mechanism or a dissociative formyl route. In the former one, CO_2 is sequentially hydrogenated to form HCOO*, formyl (HCO*), CO*, carbon (C*), and eventually carbyne (CH*) species.[15] While, in the second route, CO_2 forms $HOCO_2$* that are successively hydrogenated into HCOO*, HCO*, CO*, and ultimately CH* species.[15] Those two pathways bridged earlier kinetics with different CO_2 activation routes, raising questions about the role of OH* species and the effect of support.

In 2020, Raghu and Kaisare[16] reinforced the idea of a dissociative carbon route (CO_2* → CO* → C* → CH*) for the CO_2 methanation over Ru/TiO_2 catalyst, classifying HCOO* as spectators. They have provided theoretical justifications for previous observations, helping to contextualize divergent experimental results. At the same time, Quindimil et al.[17] have suggested that the catalytic activity of Ru-based catalysts is not exclusively a function of metal dispersion, but also of the acid-base properties of the support. More recently, Yang et al.[8] have instead proposed a reaction pathway involving HCOO* and HCO* species, followed by the formation of hydroxy-carbene (CH_2O*) and its decomposition into carbene (CH_2*), identifying C* and CH* as

potential deactivating species,[8] consistent with DFT studies. Finally, Oliveira Cabral et al.[18] have performed an in-depth study comparing three LHHW kinetic models for the CO_2 methanation over 0.6 wt.% Ru/SiO_2. They have identified the dissociative formyl route (CO_2* → CO* → HCO* → CH*) as the most consistent with experimental observations.[18] DRIFTS measurements confirmed the presence of $HOCO_2$* and HCOO* on the surface, echoing previous results,[14,15] though considering those species most likely as spectators.[18] In conclusion, when considered together, those studies seem to suggest that the mechanism of CO_2 hydrogenation to CH_4 varies depending on the acid-base properties of the support.

This work aims to compare a series of low-loaded Ru-based catalysts supported on different oxides (TiO_2, Al_2O_3, CeO_2, MgO, ZrO_2) for CO_2 methanation, to identify the most active, selective, and stable formulation. After catalytic screening, the best-performing catalyst was selected for an in-depth physicochemical and kinetic investigation supported by *operando* DRIFTS analyses. The study further aims to integrate the derived kinetic model into a real-case reactor scenario, demonstrating the potential of Ru-based catalysts for improved thermal management in CO_2 methanation processes.

2. Methodology

2.1. Catalysts Synthesis

The materials employed for the synthesis of the five catalysts, as well as the applied methodology, are detailed below. Ruthenium(III) nitrosyl nitrate ($Ru(NO)(NO_3)_x(OH)_y$, with $x + y = 3$ – 1.5 wt% Ru, Sigma-Aldrich), diluted in nitric acid, was used as the ruthenium precursor for all samples. The selected supports included γ-phase alumina (99.97% metals basis, Alfa Aesar), magnesium oxide (REMAG AC), cerium(IV) oxide (nanopowder, <25 nm particle size, SEM, Sigma-Aldrich), titanium(IV) oxide (nanopowder, 21 nm primary particle size, TEM, ≥99.5% trace metals basis, Sigma-Aldrich), and zirconium(IV) oxide (powder, 5 µm, 99% trace metals basis, Sigma-Aldrich).

All catalysts were synthesized via the incipient wetness impregnation method. In each case, 1 g of the support material was evenly dispersed to form a monolayer of particles. The ruthenium precursor, previously diluted in ultrapure water to achieve a nominal Ru loading of 0.25 wt.%, was then added dropwise periodically mixing the solid to ensure uniform distribution onto the support. Following impregnation, the samples underwent a two-step thermal treatment in a muffle furnace. Initially, they were heated to 120 °C at a rate of 2 °C/min and maintained at this temperature for 4 h to remove residual moisture. Subsequently, the temperature was increased to 500 °C at a rate of 5 °C/min and held for 5 h to promote calcination.

2.2. Catalysts Characterization

Crystallographic analysis was performed using an X'Pert PANalytical diffractometer equipped with a Cu anode radiation source ($K\alpha = 1.5418$ Å) and a PiXcel detector. Powder samples were mounted on a flat zero-background sample holder, and diffraction patterns were recorded over a 2θ range of 10° to 80°, employing Bragg–Brentano geometry. The operating conditions were set at 40 kV and 40 mA. Phase identification was carried out using the HighScore Plus software.

Nitrogen physisorption measurements at − 196 °C were conducted using a Micromeritics ASAP TRISTAR 3020 instrument. Before analysis, the catalyst samples underwent thermal pretreatment at 200 °C for 2 h in a dedicated system (Micromeritics FlowPrep 060) to remove any adsorbed species from the surface. The specific surface area (S_{BET}) was determined using the BET method within a relative pressure (P/P_0) range of 0.05 to 0.3. Additionally, pore volume and average pore size were calculated using the BJH method, applied to the desorption branch of the isotherm.

Morphological analysis was performed using a Zeiss Merlin FESEM equipped with a Gemini-II column and an Oxford X-act energy-dispersive X-ray detector to perform EDS analyses. Elemental composition and distribution were further investigated through EDS mapping. Before the analysis, a 5 nm-thick layer of platinum was deposited on the sample powders by sputter coating to enhance conductivity. Moreover, TEM measurements were carried out employing a Thermo Scientific Talos F200X microscope working at 200 kV, equipped with an EDS detector for measuring the elemental composition in STEM mode. The analyzed samples were suspended in high-purity propan-2-ol and then dripped on a holey carbon film of a copper grid support.

CO_2-TPD analysis was conducted using an Altamira AMI-300Lite chemisorption analyzer. Approximately 100 mg of catalyst powder was loaded into a quartz reactor and secured between two quartz wool plugs. Before analysis, the sample underwent thermal pretreatment under a He flow at 500 °C for 2 h. Following this step, the reactor was cooled to 50 °C, and CO_2 adsorption was carried out by exposing the sample to a flow of pure CO_2 (30 mL/min) for 60 min to ensure surface saturation. Subsequently, weakly bound CO_2 species were removed by purging the system with helium at 50 °C for 30 min. Desorption was then performed by heating the sample to 500 °C at a rate of 10 °C/min under a continuous helium flow of 30 mL/min.

H_2-TPR experiments were also performed using the same setup. For this analysis, 50 mg of the catalyst were first preconditioned in a He stream by heating to 500 °C at a rate of 10 °C/min and maintaining this temperature for 1 h. The system was then cooled under He, and the reduction profile was recorded by increasing the temperature from 50 °C to 500 °C at a rate of 10 °C/min under a flow of 5% H_2 in Ar (30 mL/min).

CO chemisorption measurements were performed using the same Altamira AMI-300Lite instrument. Approximately 50 mg of catalyst were initially subjected to a reduction treatment under a flow of 5% H_2/Ar, by heating the sample to 300 °C at a rate of 10 °C/min and maintaining this temperature for 2 h. After reduction, the reactor was cooled to 30 °C under a He atmosphere. Subsequently, small pulses of 10% CO/He were introduced into the system via a calibrated loop (524 µL) at 30 °C. CO dosing continued until saturation of the catalyst surface was achieved, as

indicated by the stabilization of the signal. The dispersion of Ru (D_{Ru}) was then calculated based on the amount of chemisorbed CO using Equation (4), assuming a spherical shape of the Ru particles and that CO adsorbs on Ru atoms in linear configuration ($n_{Ru/CO} = 1$).

$$D_{Ru} = n_{Ru/CO} \cdot \frac{V_{ads}}{\tilde{v}} \cdot \frac{M_{Ru}}{m_{Ru}} \quad (4)$$

2.3. *Operando* and In Situ DRIFTS and In Situ FTIR Investigations

DRIFTS experiments were conducted using a Praying Mantis Diffuse Reflectance Accessory, equipped with Praying Mantis High-Temperature Reaction Chambers. The measurements were performed using a Bruker Invenio S spectrometer, featuring a liquid N_2-cooled MCT detector. Downstream of the Praying Mantis cell, two analyzers were connected in series: a Hiden QGA quadrupole mass spectrometer and an ABB gas analyzer. The ABB system was equipped with the following detection channels: NDIR detectors for CO, CO_2, and CH_4, and a TCD for H_2. IR spectra were acquired with a resolution of 2 cm^{-1}, using 32 scans over the spectral range of 400–4000 cm^{-1}. The reference background spectrum was recorded over KBr powder previously dried under a 3 NL h^{-1} N_2 flow at 110 °C and atmospheric pressure. The DRIFTS measurements were performed using an internal standard approach, which is shown in Section 1 of the Supporting Information.[19–21] $CaCO_3$ was employed as the internal standard and physically mixed with each sample in an approximate maximum amount of 5 wt.%. Approximately 20 mg of the resulting catalyst–$CaCO_3$ mixture was loaded into the DRIFTS cell for each test. Finally, *operando* DRIFTS analyses were carried out only on the catalyst that exhibited the highest performance in the catalytic tests.

The catalyst was pretreated in a 10 vol.% H_2/N_2 flow (6 NL h^{-1}) at 360 °C, using a heating rate of 10 °C/min, and maintained at this temperature for 2 h. Subsequently, the cell was cooled to 200 °C, at which point the measurements were carried out. Different types of experiments were performed on the sample. *Operando* DRIFTS experiments were performed using $H_2/CO_2/N_2$ mixtures (total flow: 3 NL h^{-1}) with either a stoichiometric ratio (4/1/15) or an H_2-rich ratio (14/2/9), at atmospheric pressure and temperatures between 200 and 350 °C. A schematic representation of the *operando* DRIFTS experimental procedure is provided in Figure S1. Additionally, a CO_2 adsorption DRIFTS experiment was performed at 200 °C, 100 °C, and 50 °C under ambient pressure, using a 60 vol.% CO_2/N_2 mixture (total flow: 3 NL h^{-1}). A CO adsorption experiment was also carried out at 50 °C, feeding a 7 vol.% CO/He-N_2 mixture at a total flow rate of 3 NL h^{-1}.

In situ FTIR measurements were performed using a Bruker Invenio S spectrometer equipped with a liquid N_2-cooled MCT detector. Spectra of the best-performing catalyst were recorded in transmittance mode over the 400–4000 cm^{-1} spectral range, with a resolution of 2 cm^{-1} and 64 scans per measurement. The sample was prepared by pressing the catalyst powder into a self-supported disk (pressed at 4 tons) using a Specac manual hydraulic press. The resulting disk was then placed inside a quartz FTIR cell fitted with KBr windows. Initially, a spectrum was acquired under ambient conditions. The sample was then subjected to a thermal treatment at 400 °C (heating rate: 5 °C/min, 1 h) under vacuum. At the same temperature, the catalyst was exposed to 20 mbar of H_2 for 1 h to promote Ru reduction. After this treatment, vacuum conditions were re-established, and the cell was allowed to cool to room temperature. An FTIR spectrum was then collected under vacuum. Subsequently, CO_2 was introduced into the cell at room temperature by gradually increasing the pressure up to 100 mbar. Finally, desorption was monitored by progressively decreasing the CO_2 pressure.

2.4. Catalytic Tests

The catalytic tests were performed in the test bench schematized in Figure S2. The experiments were carried out in a quartz tube reactor (i.d. 4 mm, o.d. 6 mm) jacketed in a stainless-steel tube (i.d. 10 mm, o.d. 12 mm) equipped with a coaxial thermocouple (o.d. 1 mm) and heated by an electric oven. The reactor can operate from ambient conditions to 30 bar and 500 °C and several gases can be fed (i.e., N_2, H_2, CO_2, CH_4 and CO). The gas exiting the reactor is condensed at 5 °C and then it is analyzed by using a gas-chromatographer equipped with two columns and two detectors. In parallel, a gas analyzer monitors continuously the concentration of H_2, CO_2, CO and CH_4. In brief, each catalyst load (particle range size: 250 – 500 µm) was pre-treated at 2 bar and 450 °C (+5 °C/min) flowing 96 NL g_{cat}^{-1} h^{-1} of 5 vol.% H_2/N_2 for 2 h. After that, each sample was stabilized for 18 h at 5 bar, 425 °C flowing 240 NL g_{cat}^{-1} h^{-1} of gas ($H_2/CO_2/N_2$ equal to 4/1/25). Then after stabilization, the activity of all supported Ru-based catalysts was investigated flowing 240 NL g_{cat}^{-1} h^{-1} of gas ($H_2/CO_2/N_2$ equal to 4/1/25) at 5 bar ranging the temperature from 220 °C to 400 °C.

After the preliminary screening, the 0.25 wt.% Ru/TiO_2 catalyst was selected as the most suitable for the kinetic tests. Each catalyst load was pre-treated and stabilized as previously described. Then after stabilization, kinetic tests were performed selecting one of the conditions among those reported in Table S1. The catalyst load was substituted after each temperature ramp of the kinetic tests to avoid catalyst deactivation.

The catalytic performance of each test was evaluated in terms of CO_2 conversion, CH_4 selectivity and CH_4 yield according to Equations (5), (6), and (7), respectively.

$$\zeta_{CO_2} = 1 - \frac{\dot{n}_{CO_2,out}}{\dot{n}_{CO_2,in}} = \frac{\left(\dot{n}_{CH_4,out} - \dot{n}_{CH_4,in}\right) + \left(\dot{n}_{CO,out} - \dot{n}_{CO,in}\right)}{\dot{n}_{CO_2,in}} \quad (5)$$

$$\sigma_{CH_4} = 1 - \sigma_{CO} = \frac{\left(\dot{n}_{CH_4,out} - \dot{n}_{CH_4,in}\right)}{\zeta_{CO_2} \cdot \dot{n}_{CO_2,in}} \quad (6)$$

$$\eta_{CH_4} = \zeta_{CO_2} \cdot \sigma_{CH_4} = \frac{\left(\dot{n}_{CH_4,out} - \dot{n}_{CH_4,in}\right)}{\dot{n}_{CO_2,in}} \quad (7)$$

Lastly, the turnover frequency (TOF, s^{-1}) was evaluated according to Equation (8).[22]

$$TOF = \frac{r_{CO_2} \cdot M_{Ru}}{D_{Ru} \cdot w_{Ru}} \quad (8)$$

2.5. Kinetic Modelling

Alongside the experimental campaign, the reactor was modelled in MATLAB environment as a stationary, isothermal, isobaric, pseudo-homogeneous, 1D plug flow reactor with negligible axial dispersion.[23,24] The continuity mass balance of a generic i-th component is described by Equation (9).

$$\frac{v_z}{\varepsilon_b} \cdot \frac{d\rho_i}{dz} = (1-\varepsilon_t) \cdot \rho_s \cdot \sum_{\alpha=1}^{N_r} \left(M_i \cdot \nu_{i,\alpha} \cdot r_\alpha\right) \quad (9)$$

Thermodynamic and transport properties were estimated according to the correlations reported in the literature[23,25–30] (see Sections 3 of the Supporting Information); both intraparticle and interparticle mass and heat transport criteria were verified to avoid conditions affected by transport limitations[23,31,32] (see Section 4 of the Supporting Information).

Two power-law kinetic expressions were considered for describing the CO_2 methanation process. The first one, reported in Equation (10), depends on the partial pressure of the reactants and on the distance from the equilibrium.[23] The second one, stated in Equation (11), was proposed by Falbo et al.[11] in 2018 modifying the model proposed by Lunde and Kester[10] to consider the inhibitory effect of water.

$$r_{CH_4} = k \cdot p_{CO_2}^{n_{CO_2}} \cdot p_{H_2}^{n_{H_2}} \cdot \left(1 - \frac{Q}{K_{eq}}\right) \text{PL model} \quad (10)$$

$$r_{CH_4} = \frac{k \cdot p_{CO_2}^{n} \cdot p_{H_2}^{4n}}{1 + m \cdot p_{H_2O}} \cdot \left[1 - \left(\frac{Q}{K_{eq}}\right)^{n}\right] \text{LK} - \text{WI model} \quad (11)$$

Then, seven LHHW kinetic models were derived considering the elementary reaction steps listed in Table 1. Kinetic models M1 – M3 are those proposed by Oliveira Cabral et al.:[18] (i) model M1 represents the dissociative formyl route, (ii) model M2 represents the H-assisted formate-formyl route, and (iii) model M3 represents the bicarbonate-formate-formyl route. The other three models have instead some modifications. More in detail, kinetic model M4 considers the formation of a hydroxy-carbonyl species (*COH) on the surface and its dissociation into C* and HO* as suggested by Wang et al.[15] Model M5 is analogous to model M1, but all elementary steps are considered as reversible reactions; it represents the dissociative formyl route. Model M6 considers the dissociation of the carbonyl species (CO*) into C* and O*, so it represents the dissociative carbon route as hinted by Raghu and Kasaire.[16] Lastly, Model M7, proposed by Onrubia-Calvo et al.,[33] considers the influence of two different active sites. CO_2 is adsorbed on the basic sites of the support near the metal interface, while the adsorption and dissociation of hydrogen molecules occurs on the ruthenium. Model M7 represents the H-assisted formate-formyl route, similar to model M2, and the reaction proceeds via hydrogen spillover from the metal particles.

All models were derived assuming the formation of a monomolecular adsorbed layer with negligible interactions between adsorbates, the validity of the mass action law, the uniformity of the active sites, and the hypothesis reported in Table 1. The kinetic expressions related to the models are given in Table 2 and their complete derivation is reported in Section 5 of the Supporting Information.

The equilibrium constant for the CO_2 methanation reaction is described by the Equation (17),[10] the Arrhenius' term and the van't Hoff-type adsorption terms are evaluated according to Equations (18) and (19), respectively, and the reaction quotient is evaluated according to Equation (20).

$$K_{eq} = \exp\left[\frac{28183}{T^2} + \frac{17430}{T} - 8.25365 \cdot \ln(T) + 2.80322 \cdot 10^{-3} \cdot T + 33.165\right] \quad (17)$$

$$k = k_{T_0} \cdot \exp\left[-\frac{E_A}{R} \cdot \left(\frac{1}{T} - \frac{1}{T_0}\right)\right] \quad (18)$$

$$K_i = K_{i,T_0} \cdot \exp\left[-\frac{\Delta H_i}{R} \cdot \left(\frac{1}{T} - \frac{1}{T_0}\right)\right] \quad (19)$$

$$Q = \frac{p_{CH_4} \cdot p_{H_2O}^2}{p_{CO_2} \cdot p_{H_2}^4} \quad (20)$$

The kinetic parameters of the models were obtained by minimizing the objective function reported in Equation (21). The minimization was performed employing first a genetic algorithm and then a non-linear fitting routine to refine the solution. Among all observations, outliers were excluded considering a Cook's distance greater than $4/N_e$.[23]

$$OF = \sum_{j=1}^{N_e} \sum_{i=1}^{N_c} \left(y_{i,j}^{exp} - y_{i,j}^{mod}\right)^2 \quad (21)$$

2.6. Reactor Modelling

The last part of this work focuses on the design of an industrial-scale dual-bed methanation reactor to manage thermally the methanation reactor, exploiting the advantages of two different catalysts: 0.25 wt.% Ru/TiO_2 and 24 wt.% Ni/Al_2O_3, the latter being one of the most widely used catalysts for the methanation reaction in industrial applications. According to the literature, a cooled multitube reactor has been considered.[34–36] Catalytic particles are loaded within the tubes, while the coolant medium (i.e., pressurized boiling water) circulates in the shell. This configuration ensures excellent heat transfer between the reactant mixture inside the tubes and the refrigerant fluid.[35] Thermal control of the reaction is critical, as temperature peaks can lead to catalyst deactivation phenomena; hence, the maximum temperature limit was set at 400 °C. The catalytic bed can be configured either as a single bed employing only one of the two catalysts, or as a dual-bed reactor with different catalysts.

Table 1. Reaction steps considered for the derivation of the seven LHHW models (M1–M7). For the sake of clarity (i) and (r) refer to inert and reactive CO* species, respectively. Concerning model M7, the symbol (*) refers to Ru sites for H_2 dissociation while the symbol (^) refers to CO_2 adsorption on basic site of the support near Ru/TiO_2 interface.

Step	Reaction	M1[18]	M2[18]	M3[18]	M4	M5	M6	M7
(1)	$H_{2(g)} + 2* \rightleftharpoons 2\,H*$	Reversible	Reversible	Reversible	Reversible	Reversible	Reversible	Reversible
(2)	$CO_{2(g)} + 2* \rightleftharpoons CO^*_{(i)} + O*$	Reversible	–	–	Reversible	Reversible	Reversible	–
(3)	$CO_{2(g)} + 2* \rightleftharpoons CO^*_{(r)} + O*$	Reversible	–	–	Reversible	Reversible	Reversible	–
(4)	$CO_{2(g)} + H* \rightleftharpoons HCOO*$	–	Reversible	–	–	–	–	–
(5)	$CO_{2(g)} + OH* \rightleftharpoons HOCO^*_2$	–	–	Reversible	–	–	–	–
(6)	$CO_{2(g)} + \hat{} \rightleftharpoons CO^{\hat{}}_2$	–	–	–	–	–	–	Reversible
(7)	$CO^{\hat{}}_2 + H* \rightleftharpoons HCOO^{\hat{}} + *$	–	–	–	–	–	–	Reversible – RDS
(8)	$HOCO^*_2 + H* \rightleftharpoons HCOO* + HO*$	–	–	Reversible	–	–	–	–
(9)	$HCOO* + * \rightleftharpoons CO^*_{(i)} + HO*$	–	Reversible	Reversible	–	–	–	–
(10)	$HCOO* + * \rightleftharpoons CO^*_{(r)} + HO*$	–	Reversible	Reversible	–	–	–	–
(11)	$HCOO^{\hat{}} + * \rightleftharpoons CO^{\hat{}} + HO*$	–	–	–	–	–	–	Reversible
(12)	$CO^*_{(r)} + H* \rightleftharpoons HCO* + *$	Irreversible – RDS	Irreversible – RDS	Irreversible – RDS	Reversible	Reversible – RDS	–	–
(13)	$CO^*_{(r)} + * \rightleftharpoons C* + O*$	–	–	–	–	–	Reversible – RDS	–
(14)	$CO^{\hat{}} + H* \rightleftharpoons HCO^{\hat{}} + *$	–	–	–	–	–	–	Reversible
(15)	$HCO* + H* \rightleftharpoons CH* + HO*$	Irreversible – RDS	Irreversible – RDS	Irreversible – RDS	–	Reversible	–	–
(16)	$HCO* + * \rightleftharpoons C* + HO*$	–	–	–	Irreversible – RDS	–	–	–
(17)	$HCO^{\hat{}} + H* \rightleftharpoons CH^{\hat{}} + HO*$	–	–	–	–	–	–	Reversible
(18)	$C* + H* \rightleftharpoons CH* + *$	–	–	–	Irreversible – RDS	–	Reversible	–
(19)	$CH* + H* \rightleftharpoons CH^*_2 + *$	Reversible	Reversible	Reversible	Reversible	Reversible	Reversible	–
(20)	$CH^{\hat{}} + H* \rightleftharpoons CH^{\hat{}}_2 + *$	–	–	–	–	–	–	Reversible
(21)	$CH^*_2 + H* \rightleftharpoons CH^*_3 + *$	Reversible	Reversible	Reversible	Reversible	Reversible	Reversible	–
(22)	$CH^{\hat{}}_2 + H* \rightleftharpoons CH^{\hat{}}_3 + *$	–	–	–	–	–	–	Reversible
(23)	$CH^*_3 + H* \rightleftharpoons CH_{4(g)} + 2*$	Irreversible	Irreversible	Irreversible	Irreversible	Reversible	Reversible	–
(24)	$CH^{\hat{}}_3 + H* \rightleftharpoons CH^{\hat{}}_4 + *$	–	–	–	–	–	–	Reversible
(25)	$CH^{\hat{}}_4 \rightleftharpoons CH_{4(g)} + \hat{}$	–	–	–	–	–	–	Reversible
(26)	$O* + H* \rightleftharpoons HO* + *$	Reversible	–	–	Reversible	Reversible	Reversible	–
(27)	$HO* + H* \rightleftharpoons H_2O_{(g)} + 2*$	Irreversible	Irreversible	Irreversible	Irreversible	Reversible	Reversible	–
(28)	$HO* + H* \rightleftharpoons H_2O* + *$	–	–	–	–	–	–	Reversible
(29)	$H_2O* \rightleftharpoons H_2O_{(g)} + *$	–	–	–	–	–	–	Reversible

Table 2. Reaction rate expression of the seven LHHW models (M1–M7).

Model	Reaction rate expression	Assumption	Equations
M1, M4	$r_{CH_4} = \frac{k \cdot p_{CO_2}^{0.5} \cdot p_{H_2}^{0.75}}{(1+K_H \cdot p_{H_2}^{0.5}+K_O \cdot p_{CO_2}^{0.5} \cdot p_{H_2}^{-0.25}+K_{mix} \cdot p_{CO_2}^{0.5} \cdot p_{H_2}^{0.25})^2}$	The RDS may correspond to either step (12) or (15) in model M1, and to either step (16) or (18) in model M4.	(12)
M2, M3	$r_{CH_4} = \frac{k \cdot p_{CO_2}^{0.5} \cdot p_{H_2}^{0.75}}{(1+K_H \cdot p_{H_2}^{0.5}+K_{HCOO} \cdot p_{CO_2} \cdot p_{H_2}^{0.5}+K_{mix} \cdot p_{CO_2}^{0.5} \cdot p_{H_2}^{0.25})^2}$	The RDS may correspond to either step (12) or (15) in both model M2 and model M3.	(13)
M5	$r_{CH_4} = \frac{k \cdot p_{CO_2} \cdot p_{H_2}^{1.5} \cdot p_{H_2O}^{-1} \cdot (1-Q/K_{eq})}{(1+K_H \cdot p_{H_2}^{0.5}+K_{HO} \cdot p_{H_2O} \cdot p_{H_2}^{-0.5}+K_{mix} \cdot p_{CO_2} \cdot p_{H_2} \cdot p_{H_2O}^{-1})^2}$	The RDS corresponds to step (12).	(14)
M6	$r_{CH_4} = \frac{k \cdot p_{CO_2} \cdot p_{H_2} \cdot p_{H_2O}^{-1} \cdot (1-Q/K_{eq})}{(1+K_H \cdot p_{H_2}^{0.5}+K_{HO} \cdot p_{H_2O} \cdot p_{H_2}^{-0.5}+K_{mix} \cdot p_{CO_2} \cdot p_{H_2} \cdot p_{H_2O}^{-1})^2}$	The RDS corresponds to step (13).	(15)
M7	$r_{CH_4} = \frac{k \cdot p_{CO_2} \cdot p_{H_2}^{0.5} \cdot (1-Q/K_{eq})}{(1+K_{CO_2} \cdot p_{CO_2}) \cdot (1+K_H \cdot p_{H_2}^{0.5}+K_{HO} \cdot p_{H_2O} \cdot p_{H_2}^{-0.5})}$	The RDS corresponds to step (7)	(16)

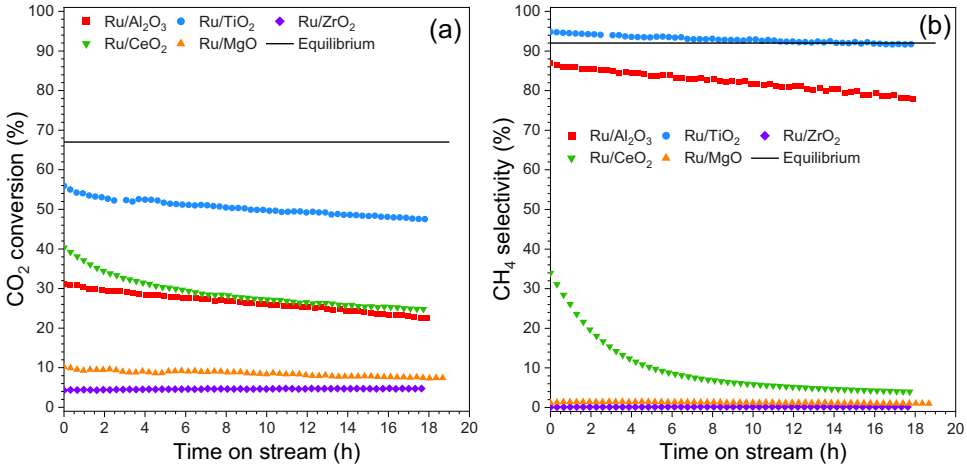

Figure 1. Time-on stream profiles of the (a) CO_2 conversion and of the (b) CH_4 selectivity during the stabilization (Reaction conditions: 5 bar, 425 °C, 60 NL/h with $H_2/CO_2/N_2$ equal to 4/1/25).

Regarding Ru/TiO_2 catalyst the LK-WI power-law kinetic expression derived in this work has been adopted (Equation 10); while the power-law expression (PL-CO_2) derived by Celoria et al. has been used for the Ni/Al_2O_3 catalyst.[23] The same simplifying assumptions presented in the previous section were also considered in this simulation. Besides the continuity mass-balance, reported in Equation (9), the heat-balance for the gaseous mixture (Equation 22) was also considered. The heat transfer coefficient was evaluated according to the correlation reported by Schlereth and Hinrichsen[27,36,37] as reported in Section 6 of the Supporting Information. The main assumptions and the geometry of the reactor are reported in Table S13.

$$v_z \cdot \rho_g \cdot \frac{\tilde{c}_{p,g}}{M_g} \cdot \frac{dT}{dz} = -\varepsilon_b \cdot (1-\varepsilon_t) \cdot \rho_s \cdot \sum_{\alpha=1}^{N_r} \left(r_\alpha \cdot \Delta_r \tilde{H}_\alpha\right) - 4 \cdot \frac{U}{d_{t,o}} \cdot (T - T_c) \tag{22}$$

3. Results and Discussion

3.1. Catalytic Screening and Characterization of the Catalysts

The five supported Ru-based catalysts were tested to determine their performance. Figure 1 shows the CO_2 conversion and CH_4 selectivity profiles during the stabilization test at 425 °C. What stands out from these tests is that the metal-support interactions have a significant impact on the activity of Ru when varying the support. Ru/ZrO_2 and Ru/MgO samples exhibited the lowest activity and CH_4 selectivity, mainly promoting the RWGS reaction. Ru/Al_2O_3 and Ru/CeO_2 showed comparable activity, but completely different CH_4 selectivity: Ru/Al_2O_3 promotes CO_2 methanation, whilst Ru/CeO_2 promotes the RWGS reaction. Lastly, the Ru/TiO_2 sample exhibited the best performance in CO_2 methanation. According to the evaluation of the turnover frequency, reported in Table 3, the catalytic activity resulted in the following performance of the supports: $TiO_2 > Al_2O_3 > CeO_2 > MgO > ZrO_2$.

All the catalysts exhibited progressive deactivation during the stabilization process; in particular, the Ru/CeO_2 sample showed the worst performance in these terms due to a significant decrease of both the CO_2 conversion and the CH_4 selectivity during the initial part of the endurance test. The other four catalysts had comparable performance in terms of stability. After stabilization, the performance of the samples was also evaluated by varying the reaction temperature from 220 °C to 400 °C and the results are illustrated in Figure S3.

To rationalize the results of the catalytic tests, textural and structural properties of the reduced catalysts were investigated. As reported in Figure S4, the XRD pattern of the Ru/MgO catalyst is characterized by the typical reflections of the cubic periclase phase (PDF 01–074–1225); similarly, both the supports of the Ru/CeO_2 and $Ru/\gamma\text{-}Al_2O_3$ catalysts exhibit a cubic crys-

Table 3. Results of the characterization of the catalysts.

Sample	Nominal Ru loading (wt.%)	BET specific surface area (m^2/g)	Total pore volume (cm^3/g)	Ru dispersion (%)	TOF (s^{-1})	CO_2-TPD (mmol/g CO_2)	H_2-TPR (mmol/g H_2)
Ru/ZrO_2	0.25	5	0.03	12.2	0.49	4.2	0.58
Ru/MgO	0.25	89	0.37	13.5	1.73	50.4	0.58
Ru/CeO_2	0.25	48	0.12	33.7	2.11	12.5	0.68
Ru/Al_2O_3	0.25	124	0.55	18.4	2.70	24.0	0.76
Ru/TiO_2	0.25	62	0.27	40.8	3.35	7.2	0.62

tal system (PDF 01–081–0792 and PDF 01–075–0921, respectively). The titanium oxide used in the preparation of the Ru/TiO_2 catalyst displays reflections corresponding to a mixture of the tetragonal anatase (PDF 01–071–1166, 71% from semi-quantitative analysis) and tetragonal rutile (PDF 01–073–2224, 29% from semi-quantitative analysis) phases. Finally, a monoclinic crystal system characterizes the support of the Ru/ZrO_2 catalyst (PDF 01–083–0940). In general, reflections attributable to the presence of metallic Ru were not observed in the XRD patterns, except in the case of γ-Al_2O_3, as the relatively low intensity of the diffractogram of this material allows the detection of highly dispersed phases. The observable reflection corresponds to the most intense peak of the metallic Ru phase, located at 44° (101), as identified by the reference pattern (PDF 01–070–0274). Regarding the TiO_2- and CeO_2-based catalysts, weak humps indicative of the presence of metallic Ru may be observed in the same angular region. The relative intensity of the ZrO_2 and MgO diffractograms is such that it prevents any detection of Ru peaks.

Concerning the N_2 physisorption measurements, all five catalysts exhibit type IV isotherms[38] (see Figure S5), which are characteristic of mesoporous materials. The hysteresis loops of the TiO_2^-, $Al_2O_3^-$, MgO^-, and CeO_2-based catalysts can be classified as type H1, which is typical of materials with well-defined cylindrical-like pore channels or agglomerates of approximately uniform spheres. The ZrO_2-based catalyst, on the other hand, corresponds to type H3, which is typical of non-rigid aggregates of plate-like particles. The specific surface area values, together with the total pore volume data, are reported in Table 3.

In the case of catalysts prepared via an impregnation method, as in the present work, active metal species are generally expected to accumulate predominantly on the surface of the support rather than within the bulk matrix. Moreover, these metal species typically exist as clusters on the support surface; consequently, only a fraction of the total deposited metal is exposed and available to participate in the catalytic reaction. The CO chemisorption technique allows for the direct quantification of surface-exposed metal atoms through the selective adsorption of gas molecules onto the metal phase. In this study, CO chemisorption was employed to determine the Ru dispersion percentage across different supports. Typically, a lower dispersion value indicates a less uniform distribution of metal species and the presence of larger metal aggregates on the surface. Ru/MgO, Ru/ZrO_2 and Ru/Al_2O_3 exhibited comparable dispersion values, all below 20%. Higher dispersion percentages were obtained for Ru/CeO_2 (33.7%) and Ru/TiO_2 (40.8%). The observed dispersion trend does not appear to correlate with the surface area of the support,[39] but rather with the redox properties of the support materials. Indeed, as shown in the H_2-TPR profiles in Figure S6a, weak interaction between Ru and the support in Ru/MgO and Ru/ZrO_2 is evident from the high-temperature reduction peaks (associated with the $RuO_2 \rightarrow Ru^0$ transition), which also appear particularly weak in the case of MgO. Conversely, Al_2O_3 and CeO_2 appear to stabilize Ru more effectively, as indicated by multiple reduction peaks at significantly lower temperatures. The presence of multiple reduction signals may suggest the coexistence of distinct Ru particle populations: (i) small and more reactive species corresponding to low-temperature peaks; and (ii) large and less reactive agglomerates reflected in high-temperature peaks. In the case of Ru/TiO_2, literature widely reports the key role played by the crystalline structure of the TiO_2 support in determining the morphology and distribution of Ru species, and consequently, the catalytic performance. In particular, Kim et al.[40] have demonstrated that a Ru/TiO_2 catalyst composed of 20% rutile and 80% anatase phases exhibits superior catalytic performance compared to catalysts supported solely on anatase or rutile TiO_2.[41] In further work, Kim et al. have reported that high Ru dispersion and particle stability are ensured through the synergistic action of several phenomena: (i) the preferential formation of thin RuO_2 layers on the rutile phase, which upon reduction are transformed into highly dispersed Ru nanoparticles;[6] and (ii) the migration of RuO_2 nanoparticles from anatase to rutile domains, where they retain high dispersion. A similar preference of Ru species for the rutile phase was also observed by Zhao et al.[6] Therefore, mixed-phase TiO_2 supports, as employed in this work, exhibit optimal characteristics for Ru dispersion because (i) the rutile phase promotes the formation of finely dispersed Ru nanoparticles, and (ii) the anatase phase serves as a reservoir for Ru species and hinders the sintering of rutile particles.[42]

The basicity of the catalysts prepared in this study was investigated using the CO_2 temperature-programmed desorption (CO_2-TPD) technique. MgO exhibited pronounced basicity, as confirmed by a broad desorption profile extending from 100 to 350 °C (Figure S6b). This feature highlights the strong tendency of magnesia to form thermally stable carbonate species. Al_2O_3 and CeO_2 displayed a more moderate basic character, with the majority of CO_2 desorbed below 200 °C. In contrast, ZrO_2 and TiO_2 showed significantly lower basicity. In particular, ZrO_2 desorbed only a minimal amount of CO_2, as also evidenced by the weak signal shown in Figure S6b. On the other hand, TiO_2 exhib-

ited some desorption signals at higher temperatures, including a notable peak around 270 °C. The quantitative data is reported in Table 3.

The surface morphology of the catalysts was investigated using Field Emission Scanning Electron Microscopy (FESEM), and the acquired images are presented in Figure S7. Overall, the catalysts do not exhibit significant morphological differences. Ru/MgO (Figure S7a) displays a heterogeneous surface composed of larger compact agglomerates dispersed within a matrix of smaller particles. This morphological heterogeneity may also be attributed to the presence of impurities formed during the synthesis process. As shown in the elemental analysis obtained by EDS (Table S14), in addition to Ru, Mg, and O, the Ru/MgO sample also contains Si, Cl, and Ca. The Ru/ZrO_2 catalyst (Figure S7b) appears more homogeneous, with geometrically shaped particles exhibiting sharp-edged surfaces. Overall, the sample seems to possess low porosity, a characteristic that is consistent with the results of nitrogen physisorption measurements at −196 °C, which were used to determine the specific surface area and porosity. Ru/Al_2O_3 (Figure S7c) is characterized by a mixture of globular and elongated particles. In contrast, Ru/CeO_2 and Ru/TiO_2 (Figure S7d,e) exhibit more homogeneous morphologies, predominantly composed of small globular particles, and a pronounced porosity.

In order to gain deeper insight into the surface structure of the samples, HR-TEM analysis was performed. The HR-TEM and HAADF-STEM images of the as-prepared Ru/TiO_2 catalyst (labelled as Ru/TiO_2_f) and spent Ru/TiO_2 (Ru/TiO_2_s) are presented in Figure 2, together with the EDS maps showing the elemental distributions of O, and Ru. As previously reported in the literature, the calcination step carried out in air promotes the formation of relatively large RuO_2 particles.[43,44] This behavior is clearly observed in the higher-magnification micrograph (Figure 2b) and in the corresponding EDS map (Figure 2c) of the as-prepared sample. In this case, RuO_2 appears as plate-like structures distributed around the titania particles, with an average agglomerate size ranging between 20 and 30 nm. In contrast, the spent sample, which underwent a reduction treatment in a H_2-rich atmosphere, exhibits a marked morphological transformation: the RuO_2 plates break down into smaller agglomerates of metallic Ru.[45,46] For this sample, well-dispersed ensembles of Ru nanoparticles are observed, as illustrated in Figure 2e and the associated EDS map (Figure 2f). Particle size analysis reveals an average Ru particle size in the range of 3 – 4 nm. These findings are consistent with the CO chemisorption analysis, which indicated a metal dispersion of 40.8%. It can therefore be concluded that ruthenium retained a good degree of dispersion despite the intense catalytic activity to which the material was subjected, confirming the structural stability of the system under demanding operational conditions.

3.2. *Operando* DRIFTS Investigations on the Ru/TiO_2 Catalyst

Operando DRIFT experiments for CO_2 methanation were performed across a temperature range from 200 °C to 350 °C under various gas feed conditions, with the aim of elucidating the hydrogenation pathway on the most active catalyst: 0.25 wt.% Ru/TiO_2. The first set of experiments under stoichiometric reaction conditions is reported in Figure 3. During the reaction, spectral bands attributed to gaseous CO_2 (2400–2250 cm^{-1}) and to the symmetric and asymmetric O–C–O stretching modes of surface carbonate species were clearly detected in the 1800–1200 cm^{-1} range. Initially, the Ru/TiO_2 catalyst surface was characterized by the presence of bidentate carbonate species, with distinct bands at 1555 and 1361 cm^{-1}, corresponding respectively to the asymmetric (ν_{asym} O–C–O) and symmetric (ν_{sym} O–C–O) stretching vibrations, separated by $\Delta\nu_3 = 188$ cm^{-1}.

A weak shoulder at 1624 cm^{-1} was also observed during the early stages of the reaction at 200 °C, potentially indicating the formation of bicarbonate ($HOCO_2$*) species. However, the other characteristic bicarbonate signals at 1400 and 1200 cm^{-1} were not detected.[47,48] As the reaction progressed, the intensity of the 1624 cm^{-1} band gradually diminished, becoming nearly undetectable at 250 °C. This suggests that hydroxyl (HO*) groups, not entirely removed during the catalyst pre-treatment at 400 °C under H_2, remained on the TiO_2 surface and reacted with CO_2 to form bicarbonate ($HOCO_2$*) intermediates. These intermediates were then progressively converted into carbonyl species, contributing to CH_4 formation.[49] Supporting this interpretation, a weak band emerged at approximately 1991 cm^{-1}, assignable to bridge-bonded CO* species.[50–53] which likely originates from the transformation of surface bicarbonates. Notably, the intensity of these carbonyl signals increased as the bicarbonate feature at 1624 cm^{-1} disappeared, particularly evident in the spectra recorded at 250 °C.

To further investigate the effect of reaction conditions, the same catalyst was tested using an over-stoichiometric gas composition halving the total flow rate. *Operando* DRIFTS spectra, displayed in Figure 4a, were collected from 200 °C to 350 °C, with corresponding catalytic data reported in Figure 4b,c. Once again, at both 200 °C and 250 °C, bands at 1562 and 1360 cm^{-1}, indicative of bidentate carbonate species, were observed. Under these more reducing conditions, however, the characteristic carbonyl band was no longer visible. This finding is consistent with previous studies by Panagiotopoulou et al.,[54] which reported a decrease in carbonyl band intensity with increasing H_2 content in the feed. The suppression of $Ru^{n+}(CO)_x$ formation was ascribed to the presence of hydrogen atoms adsorbed near Ru sites, which influence the electronic environment and reduce CO adsorption.[55,56] Increased electron density on Ru due to co-adsorbed hydrogen or carbon species enhances back-donation to CO molecules, thereby altering their adsorption behavior.

Despite the reduced accumulation of surface CO, the reaction proceeded efficiently, as confirmed by CH_4 formation detected via mass spectrometry. At 200 °C and 250 °C, CO_2 conversion increased from approximately 5% to nearly 7%, with CH_4 selectivity exceeding 99%, as shown in Figure 4b,c. At 300 °C, carbonate-related bands disappeared entirely, while a new band emerged at 3017 cm^{-1}, corresponding to the $\nu_{3,asym}$ C–H stretching mode of gaseous methane. This observation points to a rapid turnover of surface intermediates into methane under these conditions. CO_2 conversion rose sharply, surpassing 12% with CH_4 selectivity still above 99%.

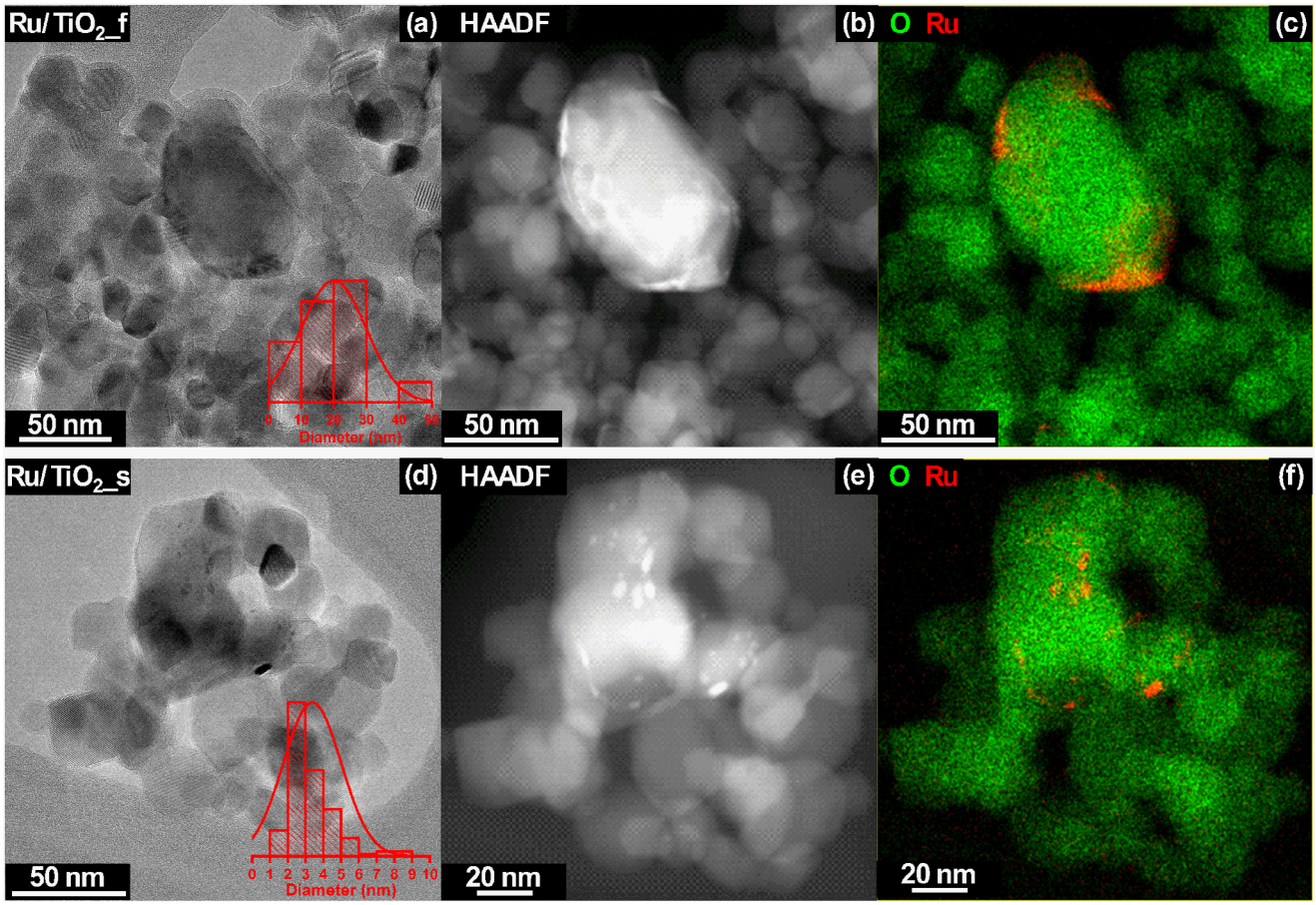

Figure 2. HR-TEM and HAADF-STEM images and STEM-EDS maps of the as-prepared Ru/TiO_2 catalyst (a – c) and of the spent Ru/TiO_2 sample (d–f).

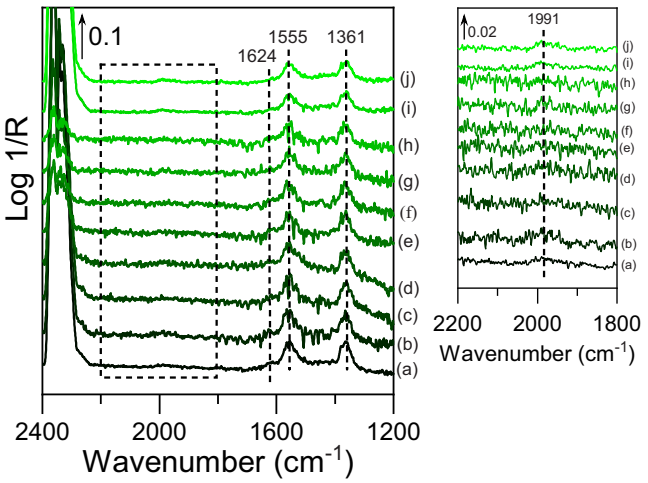

Figure 3. *Operando* DRIFTS spectra under stoichiometric reactive conditions (Reaction conditions: 1 bar, 6 NL/h with $H_2/CO_2/N_2$ equal to 4/1/15) obtained by subtracting the reference spectrum collected on the sample prior to the introduction of the reactive gas mixture (3.75 wt.% of $CaCO_3$). The temperature was set equal to 200 °C during the acquisition of spectra from (a) to (h); then it was increased to 250 °C before the acquisition of the spectra (i) and (j).

At higher temperatures, 325 °C and 350 °C, the intensity of the 3017 cm^{-1} band continued to increase, accompanied by a weak signal at 1307 cm^{-1}, attributed to the bending mode of C–H bonds in methane. These features correlated directly with enhanced CH_4 production, reaching a CO_2 conversion of over 24% at 350 °C, with a CH_4 selectivity of 98.8% and a CO selectivity of just 1.2%. Importantly, these results were achieved using only 20 mg of catalyst, including a 3.75 wt.% of $CaCO_3$, highlighting the exceptional intrinsic activity of Ru/TiO_2 and confirming its excellent performance under practical reaction conditions.

To explore the reversibility and nature of the surface species formed during reaction, the catalyst was cooled and subjected to a new feed consisting of 60 vol.% CO_2 in N_2 without H_2. Spectra were collected at 200, 100, and 50 °C, as displayed in Figure 5a. At 200 °C, no carbonate-related bands were observed, but upon cooling to 100 and 50 °C, several peaks appeared at 1670, 1581, and 1242 cm^{-1}. The 1581 cm^{-1} band (ν_{asym} OCO) is once again consistent with bidentate carbonate species.[47,48] Previous literature reports that CO_2 adsorption on TiO_2 leads to the formation of bidentate (bands at 1243 and 1670 cm^{-1}) and monodentate species (1320–1370 cm^{-1}).[57] More recent studies have attributed the bands at 1250 and 1670 cm^{-1} to carboxylate species adsorbed on Ti^{3+} centers, formed via charge transfer processes.[47,58]

To gain further insight into the formation of those surface species, an in situ FTIR experiment was conducted. As aforementioned, the Ru/TiO_2 sample underwent thermal activation under vacuum and H_2, followed by CO_2 dosing at increasing pressures up to 100 mbar. The resulting spectra (Figure 5b)

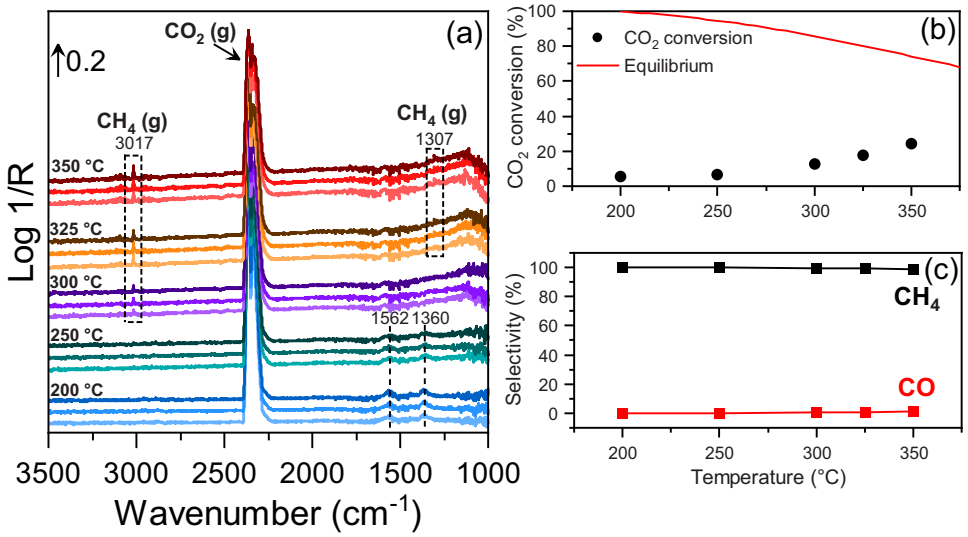

Figure 4. (a) *Operando* DRIFTS spectra were obtained by subtracting the reference spectrum collected on the sample prior to the introduction of the reactive gas mixture (3.75 wt.% of $CaCO_3$). (b) CO_2 conversion and (c) CH_4 and CO selectivity in the DRIFTS cell under reactive conditions varying the temperature from 200 °C to 350 °C (Reaction conditions: 1 bar, 3 NL/h with $H_2/CO_2/N_2$ equal to 14/2/9).

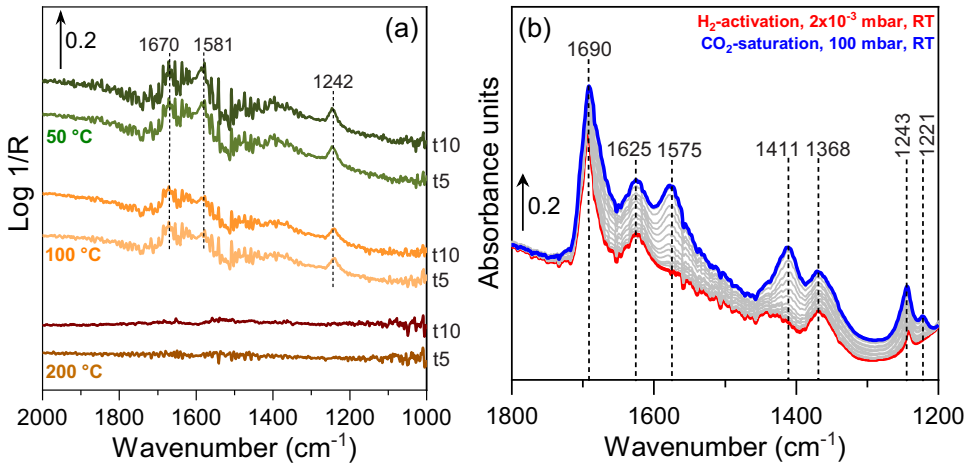

Figure 5. (a) Difference in situ DRIFTS spectra during CO_2 saturation at different temperatures (Operative conditions: 1 bar, 3 NL/h with 60 vol.% CO_2/N_2). (b) In situ FTIR spectra during CO_2 saturation at ambient temperature.

revealed a progressive emergence and intensification of vibrational features. Bands at 1690 and 1243 cm^{-1} were assigned to carboxylate species on Ti^{3+} sites, indicative of charge transfer interactions.[47,58,59] Signals at 1625, 1411, and 1221 cm^{-1} confirmed the presence of bicarbonate species, corresponding to ν_{asym} OCO, ν_{sym} OCO, and bending δ_{OH} vibrations. Additional bands at 1575 and 1368 cm^{-1} were consistent with bidentate carbonate formation.[47,48] These in situ FTIR findings align well with the in situ DRIFTS results, supporting the conclusion that bidentate carbonates are the primary surface species formed during CO_2 interaction with TiO_2. This behavior is characteristic of oxides with Lewis acid surfaces.[58,60] In contrast, bicarbonates and carboxylates seem to appear to be intermediate species, which do not accumulate significantly during reaction but are detectable under controlled IR conditions, such as those used in this study.

To further examine the surface state of Ru sites, an in situ DRIFTS experiment was performed using CO as a probe molecule. The resulting spectra (Figure S8) were dominated by gaseous CO contributions, with an additional feature in the 1900–2100 cm^{-1} range corresponding to adsorbed CO. Notably, a peak assigned to carbonyl species appeared only after 30 min of CO exposure, showing maximum intensity at t_{30} before stabilizing. The signal at 2058 cm^{-1} is attributed to linearly bonded CO arising from dissociative CO_2 adsorption on Ru.[50] As hypothesized earlier, such species are not visible under *operando* DRIFTS conditions but are revealed under CO-rich environments (7 vol.% CO). These results reinforce the notion that such species are intermediates that form during the catalytic process but do not accumulate on the surface under steady-state reaction conditions.

Table 4. Fitted kinetic parameters of the power-law kinetic models assuming the reactor isothermal (T_0 = 325 °C).

Parameter	Unit	PL model	LK-WI model
k_{T_0}	$mol\ kg_{cat}^{-1}\ s^{-1} bar^{-(n_{CO_2}+n_{H_2})}$	$(3.05 \pm 0.03) \cdot 10^{-2}$	$(3.97 \pm 0.04) \cdot 10^{-2}$
E_A	$kJ\ mol^{-1}$	46.92 ± 0.38	56.80 ± 0.36
n_{CO_2}	–	$(1.27 \pm 0.48) \cdot 10^{-2}$	–
n_{H_2}	–	0.298 ± 0.007	–
n	–	–	$(8.38 \pm 0.12) \cdot 10^{-2}$
m	bar^{-1}	–	0.97 ± 0.04

3.3. Kinetic Modeling for the Ru/TiO_2 Catalyst

As aforementioned, an in-depth investigation into the influence of different parameters was carried out to obtain a kinetic model of the 0.25 wt.% Ru/TiO_2 catalyst. Figure S9 compares the behavior of the catalyst varying different parameters: H_2 partial pressure, flowrate, catalyst loading and CO_2 partial pressure. It is worth noting that the CO_2 conversion and the CH_4 yield increase with the H_2/CO_2 ratio, rising from 4 to 10. On the contrary, CO selectivity decreases as the H_2/CO_2 ratio rises, while it increases with temperature, because the RWGS reaction is thermodynamically favored at higher temperatures. However, the CO yield remained constantly below 1%. A decrease in residence time reduced both the CO_2 conversion and the CH_4 yield, while CH_4 and CO selectivity remained nearly unaffected. Although the GHSV was kept constant, deviations from ideal plug-flow behavior in the experimental setup led to a slight increase in CH_4 yield when increasing the catalyst loading in the reactor. This fact can be ascribed to the exothermic nature of the reaction: while the generated heat approximately doubled, the overall heat transfer coefficient increased less than a factor of two. Lastly, doubling the CO_2 partial pressure resulted in an approximately halved CH_4 yield, likely due to the low order of reaction with respect to CO_2.

Moving now to the regression of the kinetic parameters, the fitted parameters of the power-law kinetic models (i.e., PL and LK-WI) are reported in Table 4. Both models lead to comparable values of the pre-exponential factors and energies of activation. More in detail, the activation energy of the LK-WI model for the Ru/TiO_2 sample is 56.8 kJ/mol, which is lower than 75.3 kJ/mol reported by Falbo et al.[11] for a Ru/Al_2O_3 catalyst. This finding is consistent with the higher activity observed for the Ru/TiO_2 catalyst compared to Ru/Al_2O_3 during the catalytic screening. In addition, the exponent n and the coefficient m in the denominator of the LK-WI model align well with those reported by Falbo et al.,[11] indicating that water inhibition also plays a role in the Ru/TiO_2 system.

Concerning the fitting, the sum of squared residuals is 0.0263 for the PL model and 0.0249 for the LK-WI model, suggesting a slightly better performance of the latter. In both cases, 15 out of 194 observations were excluded from the regression due to excessively high Cook's distance, indicating potential outliers or influential points. The parity plots of the CH_4 yield for both models are presented in Figure S10.

Turning now to the LHHW-type models (M1 – M7), the estimated kinetic parameters of the models are summarized in Table 5. Models M1 and M4 share the same reaction rate expression despite different elementary steps: M1 assumes the RDS to be the hydrogenation of CO* to HCO* (step 12) or the further hydrogenation to CH* (step 15); whereas M4 considers the dissociation of HCO* or C* hydrogenation (steps 16 or 18) as RDS. Similarly, models M2 and M3 are based on the same equation but arise from different mechanistic assumptions involving formate and bicarbonate as intermediate species. Examining the results of the fitting algorithm, models M1 and M4 provide a good fit to the experimental data with a total squared residual of 0.0243 and 13 outliers. Models M2 and M3 led instead to a slightly worse fit with 16 excluded points and a total squared residual of 0.0284. These results are consistent with the work of Oliveira Cabral et al.[18]

On the other hand, models M5 and M6 consider all elementary steps as reversible reactions including the thermodynamic driving force of the reaction but assuming different elementary steps as RDS: the CO* hydrogenation to HCO* in model M5 and the CO* dissociation into C* and O* in model M6. Both models showed a slightly higher total squared residuals (0.0307 for model M5 and 0.0301 for model M6) and a greater number of outliers (19 for model M5 and 18 for model M6). Unlike all other models, model M7 assumes that CO_2 and H_2 adsorption occurs on two different active sites of the catalyst and considers the hydrogenation of CO_2* to HCOO* as RDS. M7 provides the best fit for experimental data, with the lowest value of the objective function (0.022) and only 9 outliers. The parity plots of the CH_4 yield obtained for models M1 – M7 are illustrated in Figure S10.

In summary, although multiple mechanistic reaction pathways, model M7 emerged as the most robust and accurate representation of the CO_2 methanation kinetics on Ru/TiO_2, balancing mechanistic features and statistical performance. It supports the idea that CO_2 hydrogenation occurs via dissociative formyl route.

3.4. Industrial-Scale Dual-Bed Reactor

Although Ru-based catalysts are extremely expensive and generally considered less advantageous than Ni-based catalysts, they exhibit lower activation energy and offer better temperature control within the methanation reactor. This allows near-equilibrium CO_2 conversion (approximately 98–99%) to be reached without the need for CO_2 staging or gas recirculation through membrane separation as generally reported in the

Table 5. Fitted kinetic parameters of the LHHW kinetic models (M1 – M7) assuming the reactor isothermal (T_0 = 325 °C).

Parameter	Unit	Models M1, M4	Models M2, M3	Model M5	Model M6	Model M7
k_{T_0}	$mol\ kg_{cat}^{-1}\ s^{-1} bar^{-1.25}$	0.201 ± 0.001	0.106 ± 0.001	–	–	–
k_{T_0}	$mol\ kg_{cat}^{-1}\ s^{-1} bar^{-1.5}$	–	–	$(4.7 \pm 0.3) \cdot 10^{-2}$	–	0.43 ± 0.02
k_{T_0}	$mol\ kg_{cat}^{-1}\ s^{-1} bar^{-1}$	–	–	–	$(3.9 \pm 0.1) \cdot 10^{-3}$	–
E_A	$kJ\ mol^{-1}$	44.47 ± 0.07	33.90 ± 0.09	74.7 ± 1.1	89.2 ± 0.5	52.45 ± 2.00
K_{CO_2,T_0}	bar^{-1}	–	–	–	–	9.02 ± 0.77
ΔH_{CO_2}	$kJ\ mol^{-1}$	–	–	–	–	−2.81 ± 0.25
K_{H_2,T_0}	$bar^{-0.5}$	$(8.0 \pm 1.7) \cdot 10^{-3}$	0.208 ± 0.003	2.52 ± 0.03	0.223 ± 0.013	0.194 ± 0.008
ΔH_{H_2}	$kJ\ mol^{-1}$	−5.0 ± 0.5	−16.47 ± 0.06	−4.26 ± 0.35	−8.87 ± 0.41	−6.53 ± 0.44
K_{O,T_0}	$bar^{-0.25}$	$(2.5 \pm 0.3) \cdot 10^{-2}$	–	–	–	–
ΔH_O	$kJ\ mol^{-1}$	−8.9 ± 1.4	–	–	–	–
K_{HCOO,T_0}	$bar^{-1.5}$	–	0.540 ± 0.001	–	–	–
ΔH_{HCOO}	$kJ\ mol^{-1}$	–	−16.79 ± 0.06	–	–	–
K_{HO,T_0}	$bar^{-0.5}$	–	–	5.52 ± 0.27	1.09 ± 0.04	4.69 ± 0.21
ΔH_{HO}	$kJ\ mol^{-1}$	–	–	−19.1 ± 1.3	−8.23 ± 0.28	−1.22 ± 0.23
K_{mix,T_0}	$bar^{-0.75}$	1.735 ± 0.008	$(2.3 \pm 0.2) \cdot 10^{-8}$	–	–	–
K_{mix,T_0}	bar^{-2}	–	–	$(3.3 \pm 0.2) \cdot 10^{-2}$	$(2.6 \pm 0.1) \cdot 10^{-3}$	–
ΔH_{mix}	$kJ\ mol^{-1}$	−3.15 ± 0.05	−2.25 ± 0.02	4.24 ± 0.89	−3.21 ± 0.18	–

literature.[34–36,61–64] To prevent excessive catalyst deactivation, the reactor temperature was limited to 400 °C. As aforementioned, a single-stage reactor with Ni/Al_2O_3 catalyst, having current tubular geometry and associated heat transfer coefficients, cannot be thermally managed since very high temperatures are reached along the reactor varying either the superficial velocity of the gas (Figure S11) or the apparent density of the Ni-based catalyst (Figure S12); otherwise, the CO_2 conversion is incomplete. Hence, when using only Ni-based catalysts with a stoichiometric ($H_2/CO_2 = 4$) feed, the light-off is followed by a quick ramp of the temperature that can hardly be kept within safe limits with a conventional tubular geometry and current heat transfer coefficient.[36,62,65,66] Therefore, a dual-bed reactor was adopted, with 0.25 wt.% Ru/TiO_2 in the first part to start-up the reaction at low temperature still employing a limited Ru amount, followed by a 24 wt.% Ni/Al_2O_3 for cost-efficiency and stability.

The considered dual-bed reactor consists of 1 in (schedule 40) tubes, and the inlet gas superficial velocity was set to (0.26 ± 0.01) m/s to avoid exceeding the temperature limit, assuming 250 °C for the coolant temperature and undiluted Ru/TiO_2. Sensitivity analysis (Figure S13) shows that under these conditions, a Ru/TiO_2 bed length of 0.9 m is required to reject the reaction heat effectively and convert approximately 58% of the CO_2. It means that each tube could treat approximately 2.05 Nm^3/h of feed gas ($H_2/CO_2 = 4$), producing about 0.4 Nm^3/h of CH_4. After that, a sensitivity analysis on the apparent bed density of the Ni/Al_2O_3 section (Figure S14) indicated that, to avoid hotspots, a catalyst-to-inert ratio of 1:7 is required. The analysis showed that an apparent density of (156 ± 4) kg/m^3 is necessary to reject the reaction heat, approach thermodynamic equilibrium conversion, and keep the maximum temperature below 400 °C. Lastly, a sensitivity analysis on the coolant temperature (Figure S15) was performed to assess its influence on the thermal profiles. The results highlight that a coolant temperature of (250 ± 1) °C is required to prevent hotspots and to avoid temperature peak shifts in the second catalytic bed. Such a requirement can be easily reached with a shell side coolant operating with saturated boiling water at 250 °C and 38 bar.

Although several alternative reactor configurations could be considered depending on specific process requirements, the proposed scenario exemplifies the effective integration of a Ru-based catalyst with a Ni-based one to reduce costs while ensuring proper thermal management at the same time. Figure 6 reports the conversion and temperature profiles, accounting for fluctuations in key parameters: within approximately 2.7 m of tube length a near-equilibrium CO_2 conversion is reached, with 1/3 of the catalytic bed length filled with undiluted Ru/TiO_2 (0.9 m) and 2/3 using 24 wt.% Ni/Al_2O_3 with a catalyst-to-inert ratio of 1:7 (1.4 m). The worst scenario, where the temperature exceeds 400 °C, occurs when both the coolant temperature and gas residence time increase. However, no significant hot spots are present in the Ni-based bed. Under nominal design conditions, the peak temperature in both catalytic beds is approximately 380 °C. In conclusion, the proposed dual-bed configuration proves to be a viable and efficient solution for managing the thermal profile in CO_2 methanation reactors.

Lastly, the reactor should ensure a wide rangeability to adapt to varying operating conditions. Although the reactor geometry, catalytic beds lengths and densities are fixed during construction, the coolant temperature and the feed flowrate remain adjustable operating parameters. This flexibility can be exploited to offset either catalyst deactivation over time or manage fluctuations of the flowrate. As shown in Figure S16, a clear correlation exists between the superficial velocity and the coolant temperature required to achieve near-equilibrium CO_2 conversion,

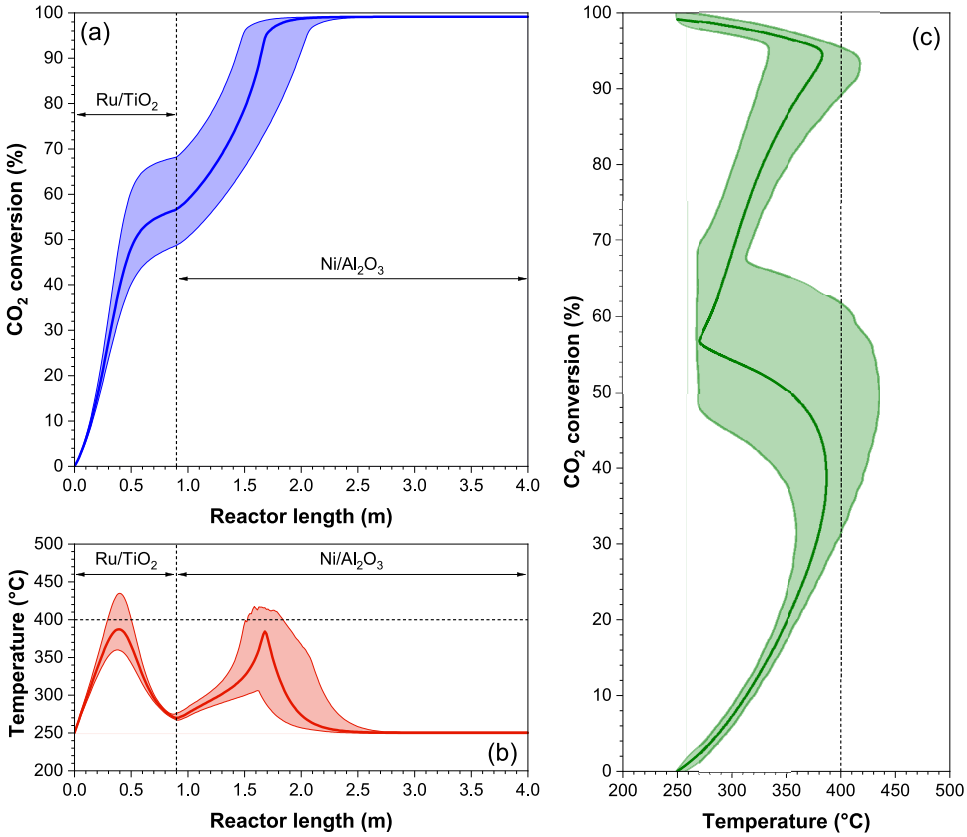

Figure 6. (a) CO_2 conversion and (b) temperature profile along the cooled industrial-scale dual-bed reactor, and (c) temperature-conversion map in the reactor considering: $v_z = (0.26 \pm 0.01)$ m · s^{-1}, $\rho_{s,\ Ni/Al_2O_3} = (156 \pm 4)$ kg · m^{-3}, $T_c = (250 \pm 1)$ °C, $\rho_{s,\ Ru/TiO_2} = 995$ kg · m^{-3}, $L_{Ru/TiO_2} = 0.9$ m, $L_t = 4$ m, $d_{t,o} = 3.35 \cdot 10^{-2}$ m, $d_{t,i} = 2.66 \cdot 10^{-2}$ m, $H_2/CO_2 = 4$. The kinetic model LK-WI was used for the Ru/TiO_2 catalyst, the kinetic model PL-CO2 was used for the Ni/Al_2O_3 catalyst, the shell-side heat transfer coefficient was assumed equal to 10 $kW \cdot m^{-2} \cdot K^{-1}$, and the tube-side heat transfer coefficient was evaluated using Schlereth's correlation.[27]

remove the produced reaction heat and limit the temperature peaks below 400 °C, within a rangeability window from 50% to 120% of the nominal gas flowrate, which corresponds to a superficial velocity of 0.26 m/s. The boiling water temperature could be controlled via its vapor pressure in the reactor shell. In conclusion, despite the challenges in thermally managing the strong exothermic CO_2 methanation reaction, the dual-bed configuration proved to be a viable alternative to the solutions reported in the literature ensuring a broad operational rangeability.

4. Conclusion

This study aimed to compare different supported low-content Ru-based catalysts for CO_2 methanation, identify and carry out an in-depth analysis of the most performant one, and employ it in a real-case scenario. The catalytic screening revealed the following order of overall performance for the supported Ru-based catalysts: $TiO_2 > Al_2O_3 > CeO_2 > MgO > ZrO_2$. Therefore, among the five impregnated Ru-based samples, the 0.25 wt.% Ru/TiO_2 catalyst exhibited superior performance in terms of stability, activity and selectivity, keeping the CO_2 conversion above 50% at 425 °C for at least 18 h with a near-equilibrium CH_4 selectivity. The characterizations revealed a dispersion of Ru atoms above 40% and a TOF of 3.35 s^{-1}. In particular, *operando* DRIFTS measurements revealed the presence of bidentate carbonate species at low temperatures (T < 300 °C), that disappeared at higher temperatures (T ≥ 300 °C), where C–H bands appeared confirming the production of CH_4. Bridge-bonded CO* species were detectable only in stoichiometric H_2/CO_2 conditions. Those pieces of information were used to derive different kinetic models, and the results of the fitting corroborate the idea that the reaction mechanism follows the dissociative formyl route. Lastly, the kinetic results were employed in a real-case scenario to show the advantages of using Ru-based catalyst to manage the thermal issues of the CO_2 methanation reactors.

Supporting Information

The authors have cited additional references within the Supporting Information.

Acknowledgments

A.R., M.P.M. and F.C. contributed equally to this work The authors kindly acknowledge the project METHA (Synthesis of renewable

METHAne from CO_2 with advanced and robust catalysts) funded by Compagnia di San Paolo through Bando "TRAPEZIO – Paving the way to research excellence and talent attraction" Linea 1: sostenere la ricerca competitiva. E.S. and F.S. acknowledge the Italian Ministry of University and Research (MUR), program FSE REACT-EU PON Ricerca e Innovazione (D.M. 1062/2021).

Conflict of Interests

The authors declare no conflict of interest.

Data Availability Statement

The data that support the findings of this study are available from the corresponding author upon reasonable request.

Keywords: CO_2 methanation · Infrared spectroscopy · Kinetic modeling · Ru/TiO_2 catalyst · Ru-based catalyst

[1] F. Solymosi, A. Erdöhelyi, M. Kocsis, *J. Chem. Soc., Faraday Trans. 1* **1981**, *77*, 1003, https://doi.org/10.1039/F19817701003.
[2] P. Panagiotopoulou, D. I. Kondarides, X. E. Verykios, *Appl. Catal. B* **2009**, *88*, 470–478, https://doi.org/10.1016/j.apcatb.2008.10.012.
[3] J. A. H. Dreyer, P. Li, L. Zhang, G. K. Beh, R. Zhang, P. H.-L. Sit, W. Y. Teoh, *Appl. Catal. B* **2017**, *219*, 715–726, https://doi.org/10.1016/j.apcatb.2017.08.011.
[4] S. López-Rodríguez, A. Davó-Quiñonero, E. Bailón-García, D. Lozano-Castelló, A. Bueno-López, *Mol. Catal.* **2021**, *515*, 111911, https://doi.org/10.1016/j.mcat.2021.111911.
[5] X. Li, J. Lin, L. Li, Y. Huang, X. Pan, S. E. Collins, Y. Ren, Y. Su, L. Kang, X. Liu, Y. Zhou, H. Wang, A. Wang, B. Qiao, X. Wang, T. Zhang, *Angew. Chem., Int. Ed.* **2020**, *59*, 19983–19989, https://doi.org/10.1002/anie.202003847.
[6] Z. Zhao, Q. Jiang, Q. Wang, M. Wang, J. Zuo, H. Chen, Q. Kuang, Z. Xie, *ACS Sustain. Chem. Eng.* **2021**, *9*, 14288–14296, https://doi.org/10.1021/acssuschemeng.1c05565.
[7] J. Zhou, Z. Gao, G. Xiang, T. Zhai, Z. Liu, W. Zhao, X. Liang, L. Wang, *Nat. Commun.* **2022**, *13*, 327, https://doi.org/10.1038/s41467-021-27910-4.
[8] C. Yang, T. Zhang, Y. Chen, W. Wang, H. Zhuo, X. Yang, Y. Huang, *ACS Catal.* **2023**, *13*, 11556–11565, https://doi.org/10.1021/acscatal.3c02502.
[9] S. Cimino, E. M. Cepollaro, L. Lisi, *Catal. Today* **2025**, *452*, 115245, https://doi.org/10.1016/j.cattod.2025.115245.
[10] P. Lunde, F. Kester, *J. Catal.* **1973**, *30*, 423–429, https://doi.org/10.1016/0021-9517(73)90159-0.
[11] L. Falbo, M. Martinelli, C. G. Visconti, L. Lietti, C. Bassano, P. Deiana, *Appl. Catal. B* **2018**, *225*, 354–363, https://doi.org/10.1016/j.apcatb.2017.11.066.
[12] G. Weatherbee, C. Barthlomew, *J. Catal.* **1982**, *77*, 460–472, https://doi.org/10.1016/0021-9517(82)90186-5.
[13] G. Weatherbee, C. Barthlomew, *J. Catal.* **1984**, *87*, 352–362, https://doi.org/10.1016/0021-9517(84)90196-9.
[14] M. Marwood, R. Doepper, M. Prairie, A. Renken, *Chem. Eng. Sci.* **1994**, *49*, 4801–4809, https://doi.org/10.1016/S0009-2509(05)80060-0.
[15] X. Wang, Y. Hong, H. Shi, J. Szanyi, *J. Catal.* **2016**, *343*, 185–195, https://doi.org/10.1016/j.jcat.2016.02.001.
[16] A. K. Raghu, N. S. Kaisare, *Ind. Eng. Chem. Res.* **2020**, *59*, 16161–16169, https://doi.org/10.1021/acs.iecr.0c02685.
[17] A. Quindimil, U. De-La-Torre, B. Pereda-Ayo, A. Davó-Quiñonero, E. Bailón-García, D. Lozano-Castelló, J. A. González-Marcos, A. Bueno-López, J. R. González-Velasco, *Catal. Today* **2020**, *356*, 419–432, https://doi.org/10.1016/j.cattod.2019.06.027.
[18] T. Oliveira Cabral, F. Bellot Noronha, F. Souza Toniolo, *Chem. Eng. J.* **2024**, *485*, 149716, https://doi.org/10.1016/j.cej.2024.149716.
[19] K. Fujiwara, S. E. Pratsinis, *Appl. Catal. B* **2018**, *226*, 127–134, https://doi.org/10.1016/j.apcatb.2017.12.042.
[20] P. Bredy, L. Fine, D. Farrusseng, Y. Schuurman, F. C. Meunier, *Catal. Today* **2023**, *424*, 114301, https://doi.org/10.1016/j.cattod.2023.114301.
[21] M. Pietro Mezzapesa, F. Salomone, E. Sartoretti, R. Pirone, S. Bensaid, F. C. Meunier, *J. Phys. Chem. C* **2025**, *129*, 8974–8984, https://doi.org/10.1021/acs.jpcc.5c01071.
[22] A. Petala, P. Panagiotopoulou, *Appl. Catal. B* **2018**, *224*, 919–927, https://doi.org/10.1016/j.apcatb.2017.11.048.
[23] F. Celoria, F. Salomone, A. Tauro, M. Gandiglio, D. Ferrero, I. Champon, G. Geffraye, R. Pirone, S. Bensaid, *Chem. Eng. J.* **2025**, *512*, 162113, https://doi.org/10.1016/j.cej.2025.162113.
[24] E. A. Morosanu, F. Salomone, R. Pirone, S. Bensaid, *Catalysts* **2020**, *10*, 283, https://doi.org/10.3390/catal10030283.
[25] B. E. Poling, J. M. Prausnitz, J. P. O'Connell, *The Properties of Gases and Liquids*, McGraw-Hill, Inc. New York **2000**.
[26] "NIST Chemistry WebBook", "NIST Chemistry WebBook," can be found under https://webbook.nist.gov/chemistry/ (accessed: October 2025).
[27] D. Schlereth, O. Hinrichsen, *Chem. Eng. Res. Des.* **2014**, *92*, 702–712, https://doi.org/10.1016/j.cherd.2013.11.014.
[28] B. Todd, J. B. Young, *J. Power Sources* **2002**, *110*, 186–200, https://doi.org/10.1016/S0378-7753(02)00277-X.
[29] R. H. Perry, D. W. Green, J. O. Maloney, *Perry's Chemical Engineers' Handbook*, 9th ed., The McGraw-Hill Companies New York **2019**.
[30] B. R. Bird, W. E. Stewart, E. N. Lightfoot, *Transport Phenomena*, John Wiley & Sons, New York **2002**.
[31] I. Champon, A. Bengaouer, A. Chaise, S. Thomas, A. C. Roger, *J. CO2 Util.* **2019**, *34*, 256–265, https://doi.org/10.1016/j.jcou.2019.05.030.
[32] D. E. Mears, *J. Catal.* **1971**, *20*, 127–131, https://doi.org/10.1016/0021-9517(71)90073-X.
[33] J. A. Onrubia-Calvo, A. Quindimil, A. Davó-Quiñonero, A. Bermejo-López, E. Bailón-García, B. Pereda-Ayo, D. Lozano-Castelló, J. A. González-Marcos, A. Bueno-López, J. R. González-Velasco, *Ind. Eng. Chem. Res.* **2022**, *61*, 10419–10435, https://doi.org/10.1021/acs.iecr.2c00164.
[34] F. Salomone, E. Giglio, D. Ferrero, M. Santarelli, R. Pirone, S. Bensaid, *Chem. Eng. J.* **2019**, *377*, 120233, https://doi.org/10.1016/j.cej.2018.10.170.
[35] E. Giglio, F. A. Deorsola, M. Gruber, S. R. Harth, E. A. Morosanu, D. Trimis, S. Bensaid, R. Pirone, *Ind. Eng. Chem. Res.* **2018**, *57*, 4007–4018, https://doi.org/10.1021/acs.iecr.8b00477.
[36] E. Giglio, P. Bruno, E. Catizzone, G. Giordano, M. Migliori, *Fuel Process. Technol.* **2025**, *276*, 108287, https://doi.org/10.1016/j.fuproc.2025.108287.
[37] P. B. Whalley, *Boiling, Condensation, and Gas-Liquid Flow*, Oxford University PressOxford Oxford **1990**, https://doi.org/10.1093/oso/9780198562344.001.0001.
[38] M. Thommes, K. Kaneko, A. V. Neimark, J. P. Olivier, F. Rodriguez-Reinoso, J. Rouquerol, K. S. W. Sing, *Pure Appl. Chem.* **2015**, *87*, 1051–1069, https://doi.org/10.1515/pac-2014-1117.
[39] J. M. González Carballo, E. Finocchio, S. García, S. Rojas, M. Ojeda, G. Busca, J. L. G. Fierro, *Catal. Sci. Technol.* **2011**, *1*, 1013, https://doi.org/10.1039/C1CY00136A.
[40] A. Kim, C. Sanchez, G. Patriarche, O. Ersen, S. Moldovan, A. Wisnet, C. Sassoye, D. P. Debecker, *Catal. Sci. Technol.* **2016**, *6*, 8117–8128, https://doi.org/10.1039/C6CY01677D.
[41] Q. Lin, X. Y. Liu, Y. Jiang, Y. Wang, Y. Huang, T. Zhang, *Catal. Sci. Technol.* **2014**, *4*, 2058–2063, https://doi.org/10.1039/C4CY00030G.
[42] A. Kim, D. P. Debecker, F. Devred, V. Dubois, C. Sanchez, C. Sassoye, *Appl. Catal. B* **2018**, *220*, 615–625, https://doi.org/10.1016/j.apcatb.2017.08.058.
[43] C. Louis, Z. X. Cheng, M. Che, *J. Phys. Chem.* **1993**, *97*, 5703–5712, https://doi.org/10.1021/j100123a040.
[44] O. U. Valdés-Martínez, C. E. Santolalla-Vargas, V. Santes, J. A. de los Reyes, B. Pawelec, J. L. G. Fierro, *Catal. Today* **2019**, *329*, 149–155, https://doi.org/10.1016/j.cattod.2018.11.007.
[45] P. Hongmanorom, V. Smeets, A. Neraud, A. Styskalik, P. Praserthdam, C. Copéret, D. P. Debecker, *Mater. Today Chem.* **2025**, *49*, 103026, https://doi.org/10.1016/j.mtchem.2025.103026.
[46] J. Kehres, J. G. Jakobsen, J. W. Andreasen, J. B. Wagner, H. Liu, A. Molenbroek, J. Sehested, I. Chorkendorff, T. Vegge, *J. Phys. Chem. C* **2012**, *116*, 21407–21415, https://doi.org/10.1021/jp3069656.

[47] J. Baltrusaitis, J. Schuttlefield, E. Zeitler, V. H. Grassian, *Chem. Eng. J.* **2011**, *170*, 471–481, https://doi.org/10.1016/j.cej.2010.12.041.
[48] C. E. Nanayakkara, W. A. Larish, V. H. Grassian, *J. Phys. Chem. C* **2014**, *118*, 23011–23021, https://doi.org/10.1021/jp504402z.
[49] S. Deng, Z. Qian, C. Zhu, B. Cheng, X. Wang, X. Fang, X. Xu, X. Wang, *ACS Catal.* **2024**, *14*, 16508–16521, https://doi.org/10.1021/acscatal.4c03801.
[50] L. M. Bravo, F. C. Meunier, J. Kopyscinski, *Appl. Catal. B: Environ. Energy* **2025**, *361*, 124591, https://doi.org/10.1039/D1CY00399B.
[51] J. Ilsemann, M. M. Murshed, T. M. Gesing, J. Kopyscinski, M. Bäumer, *Catal. Sci. Technol.* **2021**, *11*, 4098–4114, https://doi.org/10.1039/D1CY00399B.
[52] A. Rizzetto, M. Piumetti, R. Pirone, E. Sartoretti, S. Bensaid, *Catal. Today* **2024**, *429*, 114478, https://doi.org/10.1016/j.cattod.2023.114478.
[53] A. Rizzetto, E. Sartoretti, M. Piumetti, R. Pirone, S. Bensaid, *Chem. Eng. J.* **2024**, *501*, 157585, https://doi.org/10.1016/j.cej.2024.157585.
[54] P. Panagiotopoulou, D. I. Kondarides, X. E. Verykios, *Catal. Today* **2012**, *181*, 138–147, https://doi.org/10.1016/j.cattod.2011.05.030.
[55] N. M. Gupta, V. S. Kamble, R. M. Iyer, K.R. Thampi, M. Gratzel, *J. Catal.* **1992**, *137*, 473–486, https://doi.org/10.1016/0021-9517(92)90174-G.
[56] R. A. Dalla Betta, M. Shelef, *J. Catal.* **1977**, *48*, 111–119, https://doi.org/10.1016/0021-9517(77)90082-3.
[57] G. Busca, V. Lorenzelli, *Mater. Chem.* **1982**, *7*, 89–126, https://doi.org/10.1016/0390-6035(82)90059-1.
[58] W. Su, J. Zhang, Z. Feng, T. Chen, P. Ying, C. Li, *J. Phys. Chem. C* **2008**, *112*, 7710–7716, https://doi.org/10.1021/jp7118422.
[59] D. H. Gibson, *Coord. Chem. Rev.* **1999**, *185–186*, 335–355, https://doi.org/10.1016/S0010-8545(99)00021-1.
[60] G. Ramis, G. Busca, V. Lorenzelli, *Mater. Chem. Phys.* **1991**, *29*, 425–435, https://doi.org/10.1016/0254-0584(91)90037-U.
[61] E. A. Morosanu, A. Saldivia, M. Antonini, S. Bensaid, *Energy Fuels* **2018**, *32*, 8868–8879, https://doi.org/10.1021/acs.energyfuels.8b01078.
[62] E. Giglio, A. Morosanu, F. Salomone, M. Santarelli, S. Bensaid, R. Pirone, in 25th International Symposium on Chemical Reaction Engineering, Florence, **2018**.
[63] A. Mazza, F. Salomone, F. Arrigo, S. Bensaid, E. Bompard, G. Chicco, *Energy Conver. Manage.: X* **2020**, *7*, 100053, https://doi.org/10.1016/j.ecmx.2020.100053.
[64] F. Salomone, P. Marocco, D. Ferrario, A. Lanzini, D. Fino, S. Bensaid, M. Santarelli, *Appl. Energy* **2023**, *343*, 121200, https://doi.org/10.1016/j.apenergy.2023.121200.
[65] E. Giglio, R. Pirone, S. Bensaid, *Renew Energy* **2021**, *170*, 1040–1051, https://doi.org/10.1016/j.renene.2021.01.153.
[66] E. Giglio, A. Lanzini, M. Santarelli, P. Leone, *J. Energy Storage* **2015**, *1*, 22–37, https://doi.org/10.1016/j.est.2015.04.002.

Manuscript received: August 17, 2025
Revised manuscript received: October 28, 2025
Accepted manuscript online: November 23, 2025
Version of record online: ■■, ■■